



# The study of Zr adsorption on nanodispersed hydroxyapatite: X-ray photoelectron study

Yuri A. Teterin<sup>1,2</sup> · Andrey G. Kazakov<sup>1,2</sup> · Anton Yu Teterin<sup>1</sup> · Alexander V. Severin<sup>2</sup> · Stanislav V. Dvorak<sup>1</sup> · Konstantin I. Maslakov<sup>1</sup> · Kirill E. Ivanov<sup>1</sup>

Received: 28 March 2019 / Published online: 1 June 2019  
© Akadémiai Kiadó, Budapest, Hungary 2019

## Abstract

Elemental and phase composition of hydroxyapatite (HA) nanoparticle surface with absorbed zirconium were studied with X-ray photoelectron spectroscopy. Zr<sup>4+</sup> adsorption on HA nanocrystals as a function of hydrochloric solution pH was established. The mechanism of interaction of zirconium with the HA surface was discussed. The obtained results are fundamental for <sup>89</sup>Zr-based radiopharmaceuticals with a new design.

**Keywords** Zr on hydroxyapatite · X-ray photoelectron spectroscopy · Nuclear medicine

## Introduction

<sup>89</sup>Zr isotope's nuclear-physical parameters are optimal for the positron-emission tomography (PET) [1]. Relatively long half-life ( $T_{1/2} = 78.41$  h) allows application of <sup>89</sup>Zr as conjugates with antibodies relatively slow distributed along the organism. This is an advantage of <sup>89</sup>Zr compared to <sup>68</sup>Ga, <sup>64</sup>Cu, <sup>86</sup>Y, whose half-lives are lower, which does not allow the studies of slow processes in the organism [2]. At the present time <sup>89</sup>Zr is often used in PET with monoclonal antibodies [3]. <sup>89</sup>Zr-labelled antibodies proved to be effective in the clinical tests [4–6], possibility of producing of new <sup>89</sup>Zr-labelled antibodies is studied [7–10].

The main <sup>89</sup>Zr production method for nuclear medicine is <sup>nat</sup>Y (100% <sup>89</sup>Y) target irradiation on small cyclotrons [11, 12] by the <sup>89</sup>Y(p,n)<sup>89</sup>Zr and <sup>89</sup>Y(d,2n)<sup>89</sup>Zr reactions [13]. The maximal cross-section for the first reaction is 825 mb at 13.2 MeV [14], for the second one it is 950 mb at 17.2 MeV [15]. The beam energy in these reactions must be kept below the edge of the long-living <sup>88</sup>Zr formation. The yield on the thick target can reach 30 MBq·μA<sup>-1</sup>·h<sup>-1</sup> [16]

for 13 MeV protons, in the case of deuterons it can reach to 74 MBq·μA<sup>-1</sup>·h<sup>-1</sup> at 17 MeV [17].

<sup>89</sup>Zr separation from yttrium targets most often employs ion-exchange or extraction chromatography on hydroxamate resins [18]. No-carrier-added <sup>89</sup>Zr is separated in the diluted hydrochloric acid medium.

Therefore, <sup>89</sup>Zr production and separation from irradiated targets doesn't provide difficulties. However, its application in medicine is limited by complications related with insufficient strength of the complexes with bifunctional chelators. Strong binding of zirconium (coordination number 8) requires the presence of 8 electron-donating atoms in the chelator [7]. Thus, for example, the widely used in nuclear medicine chelator DTPA (diethylenetriaminepentaacetic acid) binds with zirconium <sup>89</sup>Zr with the yield of < 0.1% [19], and the binding with DOTA (1,4,7,10-tetraazacyclododecane-1,4,7,10-tetraacetic acid) requires high temperature for targeting [20].

The binding problems can be avoided by using nanoparticles with high surface area and high values of maximum adsorption. The idea is that both <sup>89</sup>Zr and the weakly bound chelator can be alternately absorbed on the nanoparticles to form a platform for the further synthesis of the radiopharmaceutical (RPC). Simultaneously high values of adsorption of the chelator and <sup>89</sup>Zr on the nanoparticles makes it possible to format a conjugate holding both the chelator and radiotracer, which are difficult to bind together directly. Besides, nanoparticles are promising as a platform for theranostic drugs, in the case when they adsorb both

✉ Yuri A. Teterin  
teterin\_ya@nrcki.ru

<sup>1</sup> Department of Nuclear and Radiation Medicine, National Research Center, Kurchatov Institute, Akademika Kurchatova pl., 1, Moscow, Russia 123098

<sup>2</sup> Chemistry Department, Lomonosov Moscow State University, Leninskie Gory, 1, Moscow, Russia 119991

the diagnostic radionuclide and the antitumor agent. As a hypothetical example one can take methotrexate absorbed on HA (which was successfully shown in [21]), if the diagnostic radionuclide is additionally adsorbed on HA.  $^{89}\text{Zr}$ -containing conjugates with monoclonal antibodies are also used as theranostic.

Literature describes effective application of nanoparticles with  $^{89}\text{Zr}$  for the RPC production. High-density lipoprotein [22] and liposomal nanoparticles [23, 24], proved to be effective in the in vivo studies as a  $^{89}\text{Zr}$  delivery system for the visualization of breast cancer tumors and mice-bearing carcinoma/papilloma. The authors of work [25] showed that gold nanoparticles can successfully serve as a platform for conjugate of  $^{89}\text{Zr}$  with the monoclonal antibody cetuximab in the PET visualization. The possibility of tumor visualization by  $^{89}\text{Zr}$ -labelled quantum dots bound with amphiphilic block copolymer was shown [26]. The obtained conjugate had high-stability in vivo, which provided high quality visualization. The possibility of visualization of conjugates based on  $\text{WS}_2/\text{WO}_x$  nanodots bound with polyethylene glycol (PEG) was also shown.  $^{89}\text{Zr}$ - $\text{WS}_2/\text{WO}_x$ -PEG conjugate is high-stability, had high labelling yield and chelator-free [27].

Also, promising nanoparticles for RPC production is nanohydroxyapatite (HA,  $\text{Ca}_{10}(\text{PO}_4)_6(\text{OH})_2$ ), which is non-toxic, biocompatible, biodegradable etc. [28]. It is known that a living organism produces biological HA as a structural component in bones. The literature describes that HA can successfully act as a carrier for medical isotopes  $^{67}\text{Zn}$  [29] and  $^{223}\text{Ra}$  [30]. The binding of HAP with radionuclides can occur by several mechanisms [31]. The bonds of the metal with the  $\text{PO}_4^{3-}$  group can form, which is likely in the case of zirconium. Zirconium ions can also replace calcium ions on the surface of HA nanoparticles. The formation of metal nanoclusters on the surface of particles is also possible.

The global goal of this work is to figure out if nanohydroxyapatite particles can be used as a “platform” for the  $^{89}\text{Zr}$  with different nuclear medicine chelators delivery. The first stage of the work is the XPS study of sorption of stable zirconium isotopes simulating the  $^{89}\text{Zr}$  isotope on HA particles. The XPS method allows the study of composition and chemical states of elements including Zr in the surface layers of HA nanocrystals.

The carrier-free  $^{89}\text{Zr}$  is separated from the irradiated targets in diluted hydrochloric acid medium. This work considers the sorption in the pH range 1.2–6.2 in chloride-ion medium in order to study the possibility of synthesis of a platform for RPC immediately after  $^{89}\text{Zr}$  separation. The data on chemical states and quantitative dependence of adsorption from pH allows a suggestion on mechanisms of tracer-nanoparticle interaction and tracer state after irradiation. Therefore, the main goal of this work was to study the composition and chemical state of elements after sorption,

in particular zirconium, in the near-surface layer of HA nanocrystals using X-ray photoelectron spectroscopy (XPS).

## Experimental

### HA nanocrystals

The present work used HA nanocrystals was produced by the method described in [32]. The nanocrystals mean parameters were  $l = (62 \pm 30)$  nm and  $d = (15 \pm 7)$  nm, while the thickness  $h$  was 1–3 HA unit cell crystallographic transmissions.

### Sample production

The samples for the XPS studies on aluminum 10 mm diameter 1 mm thick substrates were prepared as follows. Hydrochloric acid solutions of various concentrations were brought to 9 ml in a plastic vial and added to 30–50 mg of zirconium oxychloride ( $\text{ZrOCl}_2 \times 8\text{H}_2\text{O}$ ). After that, 1 ml of HA suspension (5.5 weight %) was added. After 1–2 min of mixing, pH of the solution was measured. Then, a drop of the suspension was placed on the aluminum substrate with a glass stick. The standard zirconium hydroxide sample was prepared as follows. Zirconium oxychloride was dissolved in the distilled water and added to the excess of NaOH solution. After that, a drop of the obtained suspension was placed on the aluminum substrate. The obtained samples are described in Table 1.

**Table 1** Atomic surface composition<sup>a</sup> of the samples relative to atom of P for various pH

#	Sample	Mass of $\text{ZrOCl}_2 \times 8\text{H}_2\text{O}$ , mg	pH	Surface composition <sup>b</sup>
1	HA-1	37.8	6.2	$\text{Ca}_{0.71}\text{P}_{0.60}\text{O}_{8.89}\text{C}_{0.64}\text{Zr}_{0.45}\text{Cl}_{1.47}$
2	HA-2	14.3	5.5	$\text{Ca}_{0.78}\text{P}_{0.60}\text{O}_{4.49}\text{C}_{0.34}\text{Zr}_{0.40}\text{Cl}_{1.31}$
3	HA-3	52.9	3.7	$\text{Ca}_{1.30}\text{P}_{0.60}\text{O}_{6.73}\text{C}_{0.84}\text{Zr}_{0.34}\text{Cl}_{5.12}$
4	HA-4	36.3	4.2	$\text{Ca}_{1.26}\text{P}_{0.60}\text{O}_{5.66}\text{C}_{0.86}\text{Zr}_{0.32}\text{Cl}_{3.77}$
5	HA-5	48.0	1.2	$\text{Ca}_{0.92}\text{P}_{0.60}\text{O}_{11.45}\text{C}_{1.13}\text{Zr}_{0.16}\text{Cl}_{3.77}$
6	HA	–	–	$\text{Ca}_{0.95}\text{P}_{0.60}\text{O}_{2.51+0.34}\text{C}_{0.12}\text{Ca}_{1.00}\text{P}_{0.60}\text{O}_{2.40+0.20}\text{H}_2$ (calculation)
7	$\text{Zr}(\text{OH})_4\text{-aq}$	–	–	$\text{Zr}_{1.00}\text{O}_{5.61}$

<sup>a</sup>Atomic composition by XPS relative to one P atom

<sup>b</sup>Carbon concentration for carbonate groups  $\text{CO}_3^{2-}$

## X-ray photoelectron measurements

XPS spectra of the studied HA samples were recorded on a Kratos Axis Ultra DLD spectrometer using monochromatic Al-K $\alpha$  radiation ( $h\nu = 1486.6$  eV) at 150 W X-ray gun power under  $1.3 \times 10^{-7}$  Pa at room temperature. The analyzed area was  $300 \times 700$  mm. The spectra were calibrated relative to the Au 4f $_{7/2}$  (83.96 eV) and Cu 2p $_{3/2}$  (932.62 eV) peak positions of pure gold and copper. The spectra were detected in the constant energy window using the pass energy 20 eV and step 0.05 eV. Spectrometer resolution measured as the full width at half maximum (FWHM) of the Au 4f $_{7/2}$  peak was 0.65 eV. The binding energies (BE) were measured relatively to the BE of the C 1s electrons from hydrocarbons absorbed on the sample surface that was accepted to be equal to 285.0 eV. The error in the determination of the BE and the peak width did not exceed  $\pm 0.05$  eV, and the error of the relative peak intensity was  $\pm 5\%$ . The background related with the secondary scattered electrons was subtracted by Shirley [33]. Spectral decomposition was carried out using the special program [34].

The quantitative elemental analysis was performed for several nanometer-deep layers of the studied samples [35]. It was based on the fact that the spectral intensity is proportional to the number of certain atoms in the studied sample. The following ratio was used:  $n_i/n_j = (S_i/S_j)(k_j/k_i)$ , where  $n_i/n_j$  is the relative concentration of the studied atoms,  $S_i/S_j$  is the relative core-shell spectral intensity,  $k_j/k_i$  is the relative experimental sensitivity coefficient. The following coefficients relative to the C 1s were used: 1.00 (C 1s); 2.81 (O 1s); 6.59 (Ca 2p); 1.75 (P 2p); 3.21 (Cl 2p); 9.27 (Zr 3d).

HA and Zr XPS peak were identified using the standard samples (CaO, CaCO $_3$  [36], ZrO $_2$  [37], ZrCl $_4$  [37], Zr(OH) $_4$  and ZrOCl $_2 \times 8H_2O$  [38]). In all cases, the survey and the valence band (0–50 eV BE) XPS spectra, as well as the most intense core electron spectra of zirconium, calcium, phosphorus, oxygen (O 1s) and carbon (C 1s) were measured.

## Results and discussion

### X-ray photoelectron spectra and HA surface composition

Samples 1–5 of HA (Ca $_{10}$ (PO $_4$ ) $_6$ (OH) $_2$ ) nanocrystals with absorbed zirconium were studied with the XPS method in the BE range 0–1250 eV. HA nanocrystals and Zr(OH) $_4$  on substrates were studied as standard samples. Elemental analysis was done on the basis of peak intensities with sensitivity coefficients in mind (Table 1). BEs of valence and core electrons of the included elements on the surface were measured (Table 2). Comparison with the BEs of the standard samples (6–11) was done in order to determine the oxidation states of

elements on the surfaces of Samples (1–5). XPS structures of the studied samples are given in Figs. 1, 2, 3, 4, 5, 6.

The results from Table 1 suggest a mechanism for the interaction of zirconium with HA. It is noticeable that with an increase in pH from 1.2 to 6.2, the number of zirconium atoms on the surface increases. It is also noticeable that the number of calcium atoms is reduced. This is due to the replacement of calcium ions with zirconium ions on the HA surface. Such interaction is the main mechanism in the studied conditions.

### X-ray spectra discussion

The survey XPS spectrum exhibits the peaks of included elements of Ca $_{10}$ (PO $_4$ ) $_6$ (OH) $_2$ , Zr, Cl and the C 1s peak from hydrocarbons absorbed from the air on the HA-4 sample surface (Fig. 1). The higher BE part of the spectrum shows the structure attributed to the Ca LMM, C KLL and O KLL Auger features. The low BE part shows the Al 2s and Al 2p peaks from the substrate, which indicates inhomogeneous HA and Zr adsorption on the substrate surface. The similar XPS spectra were measured for Samples (1–3, 5, 6) (Table 1).

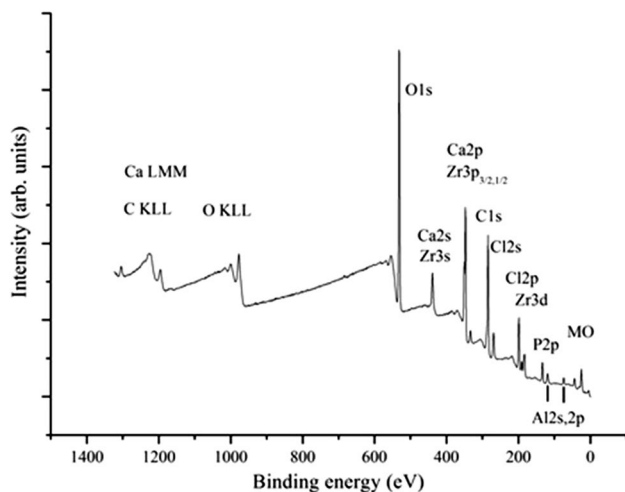
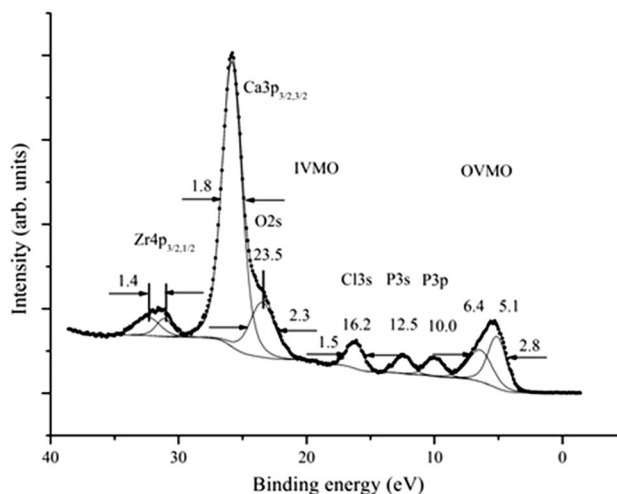
The low BE spectral range shows the features of the outer (OVMO, 0 to  $\sim 15$  eV) and the inner (IVMO,  $\sim 15$  to  $\sim 35$  eV) valence molecular orbitals (Fig. 2). The most pronounced peaks are observed in the O 2s and Ca 3p BE range. The OVMO and IVMO structure, as expected, changes with Zr adsorption. The Zr 4p peak appears and the Zr 4d $^2$  electrons make a significant contribution to the low BE spectral intensity at 5.1 and 6.4 eV (Fig. 2). The typical peak of the Cl 3s electrons is observed at 16.2 eV. At the lower BE side from the Ca 3p peak the feature attributed to the O 2s electrons participating in the chemical IVMO formation appears at 23.5 eV. This feature is widened due to participation of the O 2s electrons in the chemical bond formation. The P 3p electrons make a significant contribution to the MO structure (features at 12.5 eV and 10.0 eV). The valence band of the HA sample is 8.6 eV wide, and its structure changes during Zr adsorption. The similar XPS structure is observed in the spectra of other samples (1–3, 5) containing Zr. Therefore, one can conclude the absence on the surface of any uncontrolled impurities that could affect Zr sorption.

The sample stoichiometric composition and oxidation states of the included elements were determined on the basis of the core electron XPS peaks: Ca 2p, P 2p, Zr 3d, Cl 2p, O 1s and C 1s (see Tables 1, 2).

It has to be noted that the Zr 3d $_{5/2}$  BE of zirconium absorbed on the HA is higher than the corresponding BEs for Zr(OH) $_4$  and ZrO $_2$  and slightly lower than that for ZrOCl $_2 \times 8H_2O$  (Table 2), because zirconium on HA can be bound oxygens of the phosphate group PO $_4^{3-}$  or of the carbonate group CO $_3^{2-}$  on the surface.

**Table 2** Binding energies  $E_b$  (eV) and FWHM  $\Gamma^a$  (eV)

#	Sample	MO	Zr3d <sub>5/2</sub>	Ca2p <sub>1/2</sub>	P2p <sub>3/2</sub> P2s	Cl2p <sub>3/2</sub>	O1s	C1s
1	HA-1	5.3 7.4 10.3 12.4 16.4 23.3 25.7 31.1	183.1 (1.5)	351.3 (1.4)	133.7 (1.9) 191.1 (2.1)	198.8 (2.0)	531.8 (2.3)	285.0 (1.4) 289.0 (1.8)
2	HA-2	5.3 6.3 10.2 12.5 16.3 23.5 26.0 31.3	183.1 (2.0)	351.3 (1.4)	133.6 (2.2) 191.0 (2.3)	198.6 (2.0)	531.6 (2.5)	285.0 (1.8)
3	HA-3	5.1 6.3 10.1 12.6 16.2 24.0 26.0 31.3	183.1 (1.5)	351.5 (1.5)	133.8 (1.8) 191.1 (2.0)	198.7 (1.7)	531.9 (2.1)	285.0 (1.3) 289.0 (2.3)
4	HA-4	5.1 6.4 10.0 12.5 16.2 23.5 25.8 31.1	183.2 (1.6)	351.3 (1.5)	133.8 (1.8) 191.0 (2.2)	198.7 (1.7)	531.7 (2.0)	285.0 (1.3) 289.0 (2.6)
5	HA-5	5.1 6.5 10.3 12.5 16.1 23.7 25.9 31.4	183.3 (1.7)	351.5 (1.6)	134.1 (2.0) 191.3 (2.2)	198.6 (1.8)	532.3 (2.2)	285.0 (1.5) 289.1 (2.3)
6	HA	5.4 7.2 9.8 12.3 23.3 25.6		350.6 (1.2)	133.6 (1.5) 190.8 (2.2)		531.4 (1.2)	285.0 (1.3) 289.0 (1.3)
7	Zr(OH) <sub>4</sub> -aq	5.0 6.9 24.6 30.9	182.8 (1.3)				532.1 (2.2)	285.0 (1.3)
8	CaO [35]			349.5 (1.7)			528.9 (1.4)	285.0 (1.3)
9	CaCO <sub>3</sub> [35]			350.8 (1.7)			531.6 (1.6)	285.0 (1.3) 289.7 (1.3)
10	ZrOCl <sub>2</sub> × 8H <sub>2</sub> O [37]		183.7			199.0		285.0
11	ZrO <sub>2</sub> [37]	5.6 21.3 30.6	182.5				530.1	285.0 (1.3)
12	ZrCl <sub>4</sub> [37]		182.8			198.5		

<sup>a</sup>FWHM  $\Gamma$ (eV) in parenthesis<sup>b</sup>BE measurement error is  $\pm 0.2$  eV**Fig. 1** Survey XPS of Zr on HA: sample HA-4**Fig. 2** Valence XPS of sample HA-4

The phosphate groups in HA form stable tetrahedrons, where phosphorus state does not change for different samples. Indeed, the P 2p BE of HA does not change after zirconium adsorption. Therefore, the P 2p peak intensity was used as a standard in the quantitative analysis of Samples (1–5) (see Table 1). In this case the calcium concentration

changes as absorbed zirconium concentration increases. It yields a suggestion that zirconium partially substitutes calcium in HA.

HA, Zr(OH)<sub>4</sub>, CaO, CaCO<sub>3</sub>, ZrOCl<sub>2</sub> × 8H<sub>2</sub>O, ZrO<sub>2</sub> and ZrCl<sub>4</sub> (Table 2) were used as reference samples (6–12). The data of Table 2 show that the Zr 3d<sub>5/2</sub> BEs of Samples 1–5

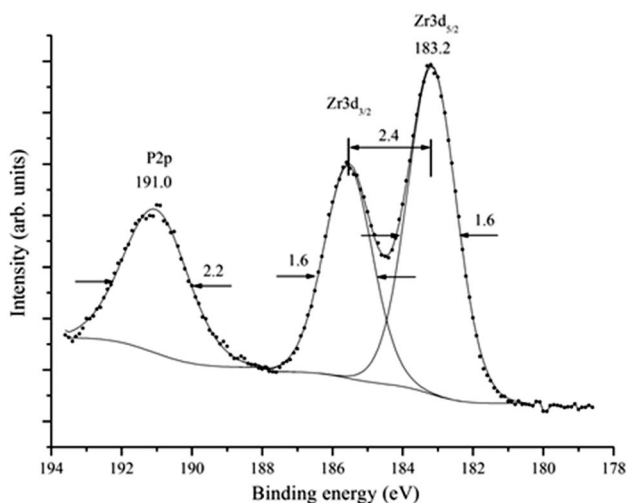


Fig. 3 Zr 3d and P 2s XPS of sample HA-4

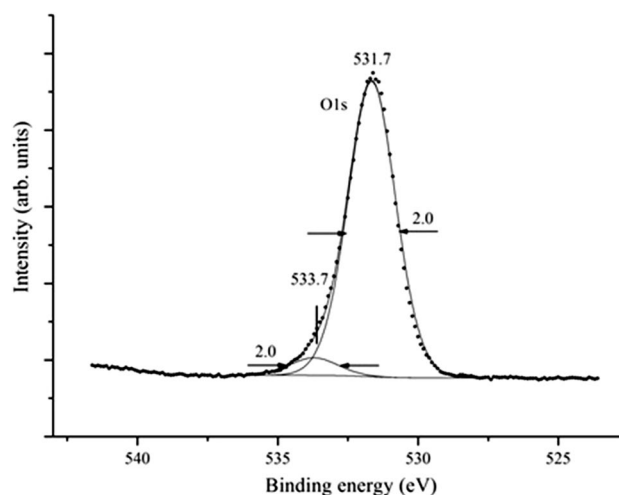


Fig. 6 O 1s XPS of sample HA-4

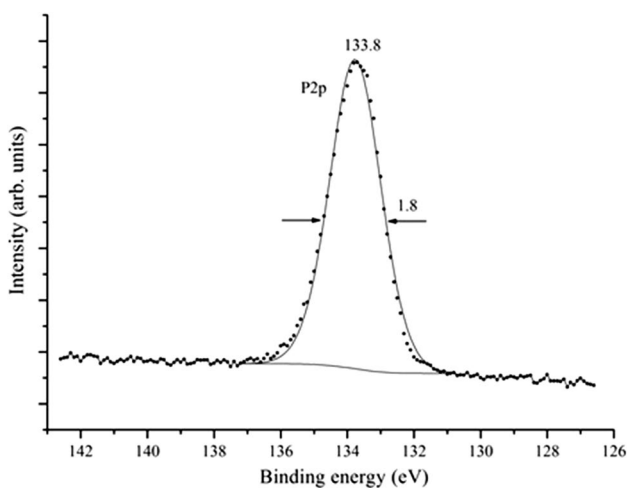


Fig. 4 P 2p XPS of sample HA-4

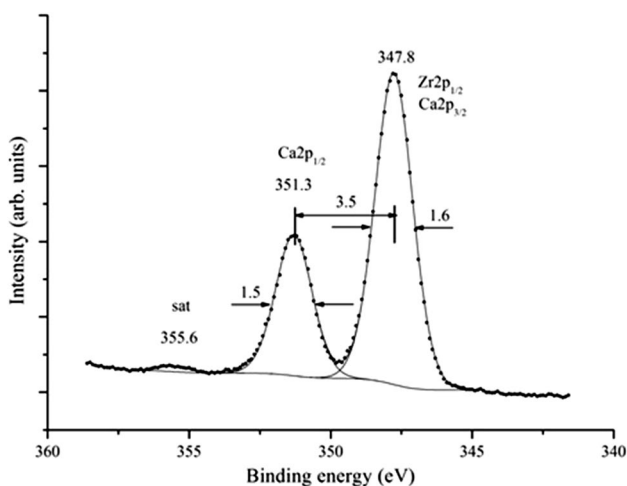


Fig. 5 Ca 2p XPS of sample HA-4

are higher than those of  $\text{ZrO}_2$ ,  $\text{Zr}(\text{OH})_4$  and  $\text{ZrCl}_4$  and lower than those of  $\text{ZrOCl}_2 \times 8\text{H}_2\text{O}$ . The Zr  $3d_{3/2}$  FWHM does not widen significantly (Table 1) as Zr surface concentration grows (Table 2). Chlorine concentration grows as pH decreases. Obviously, this can be explained by the growing of Cl concentration as pH decreases since pH is varied by the mean of hydrochloric acid. Also,  $\text{Cl}^-$  ions can substitute the hydroxyl groups in HA. It has to be noted that the error in chlorine concentration determination exceeds 10%. The pH decrease of the solution during the sample preparation lowers Zr adsorption on the surface of HA nanoparticles.

The Zr 3d peak spin–orbit splitting is  $\Delta E_{\text{sl}} = 2.4$  eV (Fig. 3). A single peak of the P 2p electrons is observed at the lower BE side from the Zr 3d doublet. These peaks intensities with photoionization cross-sections in mind allow a precise determination of the P/Zr concentration ratio.

The P 2p spectrum consists of the spin–orbit split ( $\Delta E_{\text{sl}} = 0.9$  eV) doublet [39]. However, due to phosphorus chemical nonequivalence, the P 2p spectrum exhibits a single asymmetric peak (Fig. 4).

The Ca 2p spectrum of HA consists of the spin–orbit split ( $\Delta E_{\text{sl}} = 3.5$  eV) doublet. A low intensity ( $\sim 1\%$ ) satellite due to the many-body perturbation of the Ca  $2p_{3/2}$  electrons during the photoemission is observed at the higher BE side from the Ca  $2p_{3/2}$  peak at 355.6 eV (Fig. 5). The Zr  $2p_{1/2}$  peak overlaps with the Ca 2p spectrum, which can widen the common feature. The Ca  $2p_{1/2}$  BE for Samples (1–5) does not change significantly, and it is higher than that for HA and  $\text{CaCO}_3$ .

The Cl  $2p_{3/2}$  BE for Samples (1–5) does not change significantly ( $\leq 0.3$  eV) and corresponds to that for  $\text{ZrCl}_4$ , which is typical for chlorine bound with metal (Table 2).

The C 1s spectra of Samples (1–7)  $\sim 290.0$  eV exhibit the  $\text{CO}_3^{2-}$ —related features beside the low intensity peaks at

285.0 eV of saturated hydrocarbons on the surface (Table 2). Carbon concentration of this group is given in Table 1. The  $\text{CO}_3^{2-}$  concentration changes from sample to sample, this group can participate in binding with Ca and Zr.

The O 1s spectra of Samples (1–6) exhibit a single peak with a small shoulder at the higher BE side (Fig. 6). This shoulder can be attributed to oxygen of water on the surface. The BE of 531.7 eV can be attributed to the bridge oxygen ions mostly in the P–O–P bonds with a contribution of the P–O–Ca and P–O–Zr bonds, while the BE of 533.7 eV can be attributed to water in HA and on the sample surface. The concentration of  $\text{PO}_4^{3-}$ -related oxygen, as well as water-related oxygen given as a sum (Table 1) changes as Zr adsorption on HA grows and sample preparation conditions change. Taking into account Eq. [36]:

$$R_{\text{E-O}}(\text{nm}) = 2.27 (E_b - 519.4)^{-1}, \quad (1)$$

the element-oxygen interatomic distances  $R_{\text{E-O}}$  (nm) were evaluated. For the O 1s BEs 531.7 and 533.7 eV (Table 2) the  $R_{\text{E-O}}$  are 0.185 nm and 0.159 nm characterizing the element-oxygen interatomic distances on the surface of the studied samples. These values are average for the P–O, Ca–O, Zr–O bonds. The O 1s spectrum of Sample 7 exhibits the features at 530.1 and 532.1 eV. The feature at 530.1 eV can be attributed to oxygen from  $\text{ZrO}_2$  ( $\text{O}_{0.54}$ , Table 1), and the one at 532.1 eV can be attributed to oxygen from  $\text{ZrOCl}_2 \times 8\text{H}_2\text{O}$ . Using Eq. 1 one can determine the mean interatomic distance Zr–O in  $\text{ZrO}_2$  being  $R_{\text{Zr-O}} = 0.212$  nm, which is comparable with the mean experimental value of 0.2150 nm [40].

## Conclusions

The  $\text{Zr}^{4+}$  adsorption on HA nanocrystals as a function of hydrochloric solution pH was studied by XPS method. It was found that as pH grows in the range 1.2–6.2, concentration of absorbed zirconium ions increases about thrice. A decrease in the amount of calcium in this case indicates that zirconium replaces calcium on the surface of HA nanoparticles. The results show a possibility of synthesis of  $^{89}\text{Zr}$ -HA conjugates and the most favorable conditions for this are close to the organism medium. The obtained results are fundamental for  $^{89}\text{Zr}$ -based radiopharmaceuticals with a new design using HA nanoparticles as carriers for both  $^{89}\text{Zr}$  and chelator. However, to create such radiopharmaceuticals, sorption experiments with the  $^{89}\text{Zr}$  tracer are required to supplement the obtained data.

**Acknowledgements** The authors acknowledge support from Lomonosov Moscow State University Program of Development for providing access to the XPS facility. The work was partially supported by the RFBR Grants 18-33-00649 and 17-03-00277a.

## References

1. Chu SYF, Ekström LP, Firestone RB. WWW table of radioactive isotopes. In: Database version 1999-02-28
2. Deri MA, Zeglis BM, Francesconi LC, Lewis JS (2013) PET imaging with  $^{89}\text{Zr}$ : from radiochemistry to the clinic. *Nucl Med Biol* 40:3–14. <https://doi.org/10.1016/j.nucmedbio.2012.08.004>
3. Moek KL, Giesen D, Kok IC et al (2017) Theranostics using antibodies and antibody-related therapeutics. *J Nucl Med* 58:83S–90S. <https://doi.org/10.2967/jnumed.116.186940>
4. Rice SL, Roney CA, Daumar P, Lewis JS (2011) The next generation of positron emission tomography radiopharmaceuticals in oncology. *Semin Nucl Med* 41:265–282. <https://doi.org/10.1053/j.semnuclmed.2011.02.002>
5. Jauw YW, der Houven Menke-van, van Oordt CW, Hoekstra OS et al (2016) Immuno-positron emission tomography with zirconium-89-labeled monoclonal antibodies in oncology: what can we learn from initial clinical trials? *Front Pharmacol* 7:1–15. <https://doi.org/10.3389/fphar.2016.00131>
6. van de Watering FCJ, Rijpkema M, Perk L et al (2014) Zirconium-89 labeled antibodies: a new tool for molecular imaging in cancer patients. *Biomed Res Int* 2014:1–13. <https://doi.org/10.1155/2014/203601>
7. Heskamp S, Raavé R, Boerman OC et al (2017)  $^{89}\text{Zr}$ -immuno-PET in oncology: state of the art  $^{89}\text{Zr}$ -radiochemistry. *Bioconjug Chem*. <https://doi.org/10.1021/acs.bioconjugchem.7b00325>
8. Jansen MH, Veldhuijzen van Zanten SEM, van Vuurden DG et al (2017) Molecular drug imaging:  $^{89}\text{Zr}$ -bevacizumab PET in children with diffuse intrinsic pontine glioma. *J Nucl Med* 58:711–716. <https://doi.org/10.2967/jnumed.116.180216>
9. Price EW, Carnazza KE, Carlin SD et al (2017)  $^{89}\text{Zr}$ -DFO-AMG102 immuno-PET to determine local hepatocyte growth factor protein levels in tumors for enhanced patient selection. *J Nucl Med* 58:1386–1394. <https://doi.org/10.2967/jnumed.116.187310>
10. van Es SC, Brouwers AH, Mahesh SVK et al (2017)  $^{89}\text{Zr}$ -bevacizumab PET: potential early indicator of everolimus efficacy in patients with metastatic renal cell carcinoma. *J Nucl Med* 58:905–910. <https://doi.org/10.2967/jnumed.116.183475>
11. Holland JP, Sheh Y, Lewis JS (2009) Standardized methods for the production of high specific-activity zirconium-89. *Nucl Med Biol* 36:729–739. <https://doi.org/10.1016/j.nucmedbio.2009.05.007>
12. Severin GW, Jørgensen JT, Wiehr S et al (2015) The impact of weakly bound  $^{89}\text{Zr}$  on preclinical studies: non-specific accumulation in solid tumors and aspergillus infection. *Nucl Med Biol* 42:360–368. <https://doi.org/10.1016/j.nucmedbio.2014.11.005>
13. Krasikova RN, Aliev RA, Kalmykov SN (2016) The next generation of positron emission tomography radiopharmaceuticals labeled with non-conventional radionuclides. *Mendeleev Commun* 26:85–94. <https://doi.org/10.1016/j.mencom.2016.03.001>
14. Ciarmatori A, Cicoria G, Pancaldi D et al (2011) Some experimental studies on  $^{89}\text{Zr}$  production. *Radiochim Acta* 99:631–634. <https://doi.org/10.1524/ract.2011.1822>
15. Degering D, Unterricker S, Stolz W (1988) Excitation function of the  $^{89}\text{Y}(d,2n)^{89}\text{Zr}$  reaction. *J Radioanal Nucl Chem Lett* 127(1):7–11
16. Kandil SA, Scholten B, Saleh ZA et al (2007) A comparative study on the separation of radiozirconium via ion-exchange and solvent extraction techniques, with particular reference to the production of  $^{88}\text{Zr}$  and  $^{89}\text{Zr}$  in proton induced reactions on yttrium. *J Radioanal Nucl Chem* 274:45–52. <https://doi.org/10.1007/s10967-006-6892-2>
17. Zweit J, Downey S, Sharma HL (1991) Production of no-carrier-added zirconium-89 for positron emission tomography. *Int J Radiat Appl Instrum Part A Appl Radiat Isot* 42:199–201. [https://doi.org/10.1016/0883-2889\(91\)90074-B](https://doi.org/10.1016/0883-2889(91)90074-B)

18. Kasbollah A, Eu P, Cowell S, Deb P (2013) Review on production of  $^{89}\text{Zr}$  in a medical cyclotron for PET radiopharmaceuticals. *J Nucl Med Technol* 41:35–41. <https://doi.org/10.2967/jnmt.112.111377>
19. Perk LR, Visser OJ, Stigter-Van Walsum M et al (2006) Preparation and evaluation of  $^{89}\text{Zr}$ -Zevalin for monitoring of  $^{90}\text{Y}$ -Zevalin biodistribution with positron emission tomography. *Eur J Nucl Med Mol Imaging* 33:1337–1345. <https://doi.org/10.1007/s00259-006-0160-0>
20. Pandya DN, Pailloux S, Tatum D et al (2015) Di-macrocyclic terphthalamide ligands as chelators for the PET radionuclide zirconium-89. *Chem Commun* 51:2301–2303. <https://doi.org/10.1039/C4CC09256B>
21. Meshkini A, Oveisi H (2017) Methotrexate-F127 conjugated mesoporous zinc hydroxyapatite as an efficient drug delivery system for overcoming chemotherapy resistance in osteosarcoma cells. *Colloids Surf. B Biointerfaces* 158:319–330. <https://doi.org/10.1016/j.colsurfb.2017.07.006>
22. Perez-Medina C, Tang J, Abdel-Atti D et al (2015) PET imaging of tumor-associated macrophages with  $^{89}\text{Zr}$ -labeled high-density lipoprotein nanoparticles. *J Nucl Med* 56:1272–1277. <https://doi.org/10.2967/jnumed.115.158956>
23. Perez-Medina C, Abdel-Atti D, Zhang Y et al (2014) A modular labeling strategy for in vivo PET and near-infrared fluorescence imaging of nanoparticle tumor targeting. *J Nucl Med* 55:1706–1711. <https://doi.org/10.2967/jnumed.114.141861>
24. Li N, Yu Z, Pham T et al (2017) A generic  $^{89}\text{Zr}$  labeling method to quantify the in vivo pharmacokinetics of liposomal nanoparticles with positron emission tomography. *Int J Nanomed* 12:3281–3294. <https://doi.org/10.2147/IJN.S134379>
25. Zhao Y, Shaffer TM, Das S et al (2017) Near-infrared quantum dot and  $^{89}\text{Zr}$  dual-labeled nanoparticles for in vivo Cerenkov imaging. *Bioconjug Chem* 28:600–608. <https://doi.org/10.1021/acs.bioconjchem.6b00687>
26. Karmani L, Labar D, Valembois V et al (2013) Antibody-functionalized nanoparticles for imaging cancer: influence of conjugation to gold nanoparticles on the biodistribution of  $^{89}\text{Zr}$ -labeled cetuximab in mice. *Contrast Media Mol Imaging* 8:402–408. <https://doi.org/10.1002/cmmi.1539>
27. Cheng L, Kamkaew A, Shen S et al (2016) Facile preparation of multifunctional  $\text{WS}_2/\text{WO}_x$  nanodots for chelator-free  $^{89}\text{Zr}$ -labeling and in vivo PET imaging. *Small* 12:5750–5758. <https://doi.org/10.1002/sml.201601696>
28. Kolmas J, Krukowski S, Laskus A, Jurkitewicz M (2016) Synthetic hydroxyapatite in pharmaceutical applications. *Ceram Int* 42:2472–2487. <https://doi.org/10.1016/j.ceramint.2015.10.048>
29. Orlova MA, Nikolaev AL, Trofimova TP et al (2019) Hydroxyapatite and porphyrin-fullerene nanoparticles for diagnostic and therapeutic delivery of paramagnetic ions and radionuclides. *Bull Russ State Med Univ*. <https://doi.org/10.24075/brsmu.2018.075>
30. Vasiliev AN, Severin A, Lapshina E et al (2017) Hydroxyapatite particles as carriers for  $^{223}\text{Ra}$ . *J Radioanal Nucl Chem* 311:1503–1509. <https://doi.org/10.1007/s10967-016-5007-y>
31. Severin AV, Pankratov DA (2016) Synthesis of nanohydroxyapatite in the presence of iron(III) ions. *Russ J Inorg Chem* 61:265–272. <https://doi.org/10.1134/s0036023616030190>
32. Melikhov IV, Komarov VF, Severin AV (2000) Two-dimensional crystal hydroxyapatite. *Rep Russ Acad Sci* 373:355 (In Russian)
33. Shirley DA (1972) High-resolution X-ray photoemission spectrum of the valence bands of gold. *Phys Rev B* 5:4709–4714. <https://doi.org/10.1103/PhysRevB.5.4709>
34. Panov AD (1997) Packet of programs of spectra processing SPRO and programming language SL. Prepr Inst At Energy, Moscow, IAE-6019/15 31
35. Nemoshkalenko VV (1976) Electron spectroscopy of crystals. Naukova Du, Moscow
36. Sosulnikov MI, Teterin YA (1992) X-ray photoelectron studies of Ca, Sr and Ba and their oxides and carbonates. *J Electron Spectrosc Relat Phenomena* 59:111–126. [https://doi.org/10.1016/0368-2048\(92\)85002-0](https://doi.org/10.1016/0368-2048(92)85002-0)
37. Maslakov KI, Livshits TS, Lapina MI et al (2007) An X-ray photoelectron study of the  $(\text{Ca}_{2.5}\text{Th}_{0.5})\text{Zr}_2\text{Fe}_3\text{O}_{12}$ ,  $(\text{Ca}_{1.5}\text{GdTh}_{0.5})(\text{ZrFe})\text{Fe}_3\text{O}_{12}$ , and  $(\text{Ca}_{2.5}\text{Ce}_{0.5})\text{Zr}_2\text{Fe}_3\text{O}_{12}$  ceramics with a garnet structure. *Radiochemistry* 49:33–40. <https://doi.org/10.1134/s1066362207010067>
38. Nefedov VI (1985) X-ray spectroscopy of chemical compounds. Himiya, Moscow
39. Trzhaskovskaya MB, Yarzhemsky VG (2018) Dirac–Fock photoionization parameters for HAXPES applications. *At Data Nucl Data Tables* 119:99–174. <https://doi.org/10.1016/j.adt.2017.04.003>
40. Smith DK, Newkirk HW (1965) The crystal structure of baddeleyite (monoclinic  $\text{ZrO}_2$ ) and its relation to the polymorphism of  $\text{ZrO}_2$ . *Acta Crystallogr* 18:983–985

**Publisher's Note** Springer Nature remains neutral with regard to jurisdictional claims in published maps and institutional affiliations.